



# CFD-DEM investigation of particles circulation pattern of two-tower fluidized bed reactor for beam-down solar concentrating system

Selvan Bellan<sup>a,c,\*</sup>, Koji Matsubara<sup>b,c</sup>, Cho Hyun Cheok<sup>a,c</sup>, Nobuyuki Gokon<sup>a,c</sup>, Tatsuya Kodama<sup>b,c</sup>

<sup>a</sup> Center for Transdisciplinary Research, Niigata University, 8050 Ikarashi 2-nocho, Niigata 950-2181, Japan

<sup>b</sup> Faculty of Engineering, Niigata University, 8050 Ikarashi 2-nocho, Niigata 950-2181, Japan

<sup>c</sup> Pacific Rim Solar Fuel System Research Center, Niigata University, 8050 Ikarashi 2-nocho, Niigata 950-2181, Japan

## ARTICLE INFO

### Article history:

Received 15 February 2017

Received in revised form 19 May 2017

Accepted 28 June 2017

Available online 30 June 2017

### Keywords:

Solar receiver

CFD-DEM modeling

Fluidized bed

Particle-fluid flow

Beam-down solar concentrating system

## ABSTRACT

In this study, a numerical model has been developed by the combined approach of computational fluid dynamics (CFD) and discrete element method (DEM) collisional model to study the particle-fluid flow of the fluidized bed reactor for solar beam-down concentrating system. The contact forces between the particles have been calculated by the spring-dashpot model, based on the soft-sphere method. An experimental visualization of particles circulation pattern and mixing of two-tower fluidized bed system has been presented. A good agreement has been found between the experimental measurements and numerical predictions. To investigate the influence of fluid flow rate and particle size on the flow pattern of the reactor, simulations have been performed for various conditions. The results indicate that the large size particles induce three-dimensional effects as they are accumulated at the central axis region. The average bed height of the left tower increased by 23.4% when increasing the flow rate about 70%.

© 2017 Elsevier B.V. All rights reserved.

## 1. Introduction

Fluidized bed technology is widely used in various industrial applications, including mechanical and chemical industries, due to its superior heat and mass transfer characteristics. Fluidized bed reactors have been used as reactor/receiver and storage systems of concentrated solar plants, which is one of the promising technologies currently undergoing rapid development [1–4]. Solar particle receivers (SPR) were developed to drive the concentrating solar plants (CSP) towards higher operating temperatures and enhance the efficiency of the power cycles. The SPR-based CSP system uses solid particles as the heat transfer medium (HTM) in place of currently used molten salt or steam [5–7]. An experimental and theoretical study of a pilot scale solar fluidized bed receiver was carried out by Flamant et al. [5] at the early stage of development using alumina particles, and the unsteady behavior of the receiver in the temperature range of 550–915 °C was described by a simple heat transfer model. Recently, a tubular fluidized receiver for beam-down solar concentrating system was developed by Matsubara et al. [8]. The fluid dynamics of the prototype receiver was experimentally investigated by 3 kW<sub>th</sub> solar simulator. Subsequently, a two-tower fluidized receiver was developed for beam down system and an experimental visualization of cold particle-flow prototype was presented [9]. In concentrated solar thermal industry, fluidized-bed technology has also been

used to produce hydrogen by thermochemical two step water splitting cycles [2], and synthetic gas by gasification of coal coke [10].

The hydrodynamic behavior of the gas-solid flow plays a vital role in the aforementioned fluidized bed reactors. Thus, in order to measure and study the dynamics of dense gas-solid flow, different kind of techniques have been developed such as particle image velocimetry (PIV), digital image analysis (DIA), positron emission particle tracking, magnetic resonance imaging, electrical capacitance tomography, and etc. However, it's pretty challenging to obtain accurate flow characteristics at reasonable cost [11]. With rapid advancements of computers and numerical algorithms, CFD has become a powerful tool to obtain the flow characteristics of the dense gas-solid flow qualitatively. Various numerical models have been developed in the past few decades to simulate the gas-solid flows. The most widely used models are Eulerian-Eulerian and Eulerian-Lagrangian models. The Eulerian-Eulerian model treats both gas and solid phases as continuum, and uses the kinetic theory of granular flow to calculate the solid phase pressure and viscosity. The Eulerian-Lagrangian (CFD-DEM or CFD-DPM) model accounts the motion of each particle individually in the continuum gas phase. Therefore, the CFD-DEM model is computationally expensive.

In discrete particle model, the particle collisions can be either modelled by soft sphere or hard sphere approach. In hard-sphere (binary collision) approach, collision between two particles or between a particle and the wall is evaluated separately; which is an event driven model since the particles are moved until the next collision occurs. The soft-sphere model is driven by a time step as the particles are moved together with a fixed time step; which allows overlap between the particles and

\* Corresponding author.

E-mail address: [selvan@eng.niigata-u.ac.jp](mailto:selvan@eng.niigata-u.ac.jp) (S. Bellan).

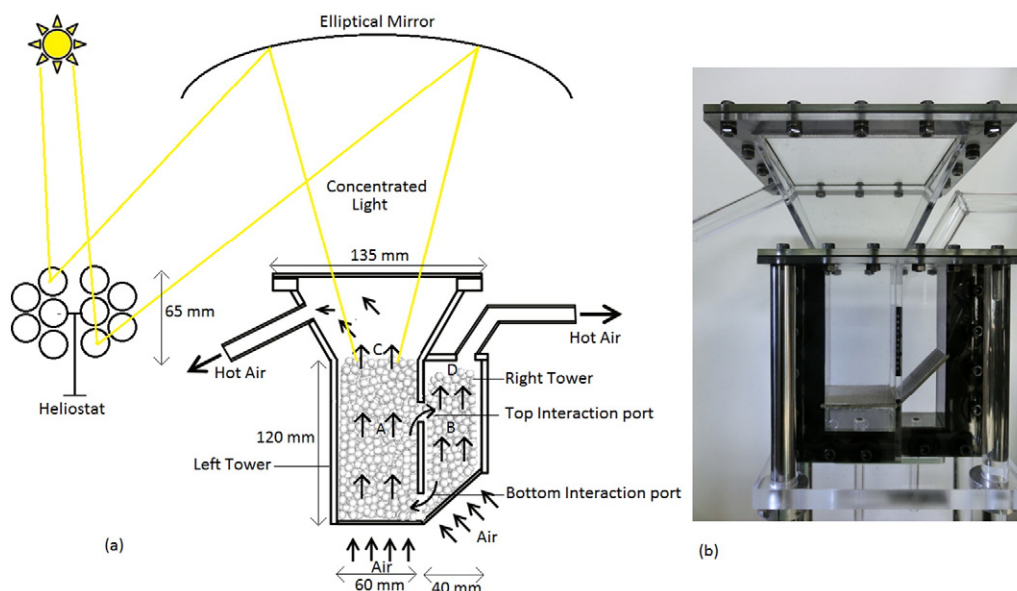


Fig. 1. (a) Schematic of the beam-down concentrated receiver/reactor and (b) transparent experimental setup.

calculates a contact force between the particles by spring-dashpot approach [12]. Initially, Tsuji et al. [13] developed a two dimensional CFD-DEM model for fluidized bed by soft sphere approach. Following their study, various researchers have improved that model extensively with some modifications in the past two decades. In the early stages, the number of simulation particles was several thousand only but now with the vast improved computers and techniques, up to 100,000 particles can be simulated with single core processor. By parallel computing, fluidized bed systems consisting of several million particles have been simulated for different kinds of problems [14,15]. Multi-physics problems coupled with heat transfer and chemical reactions were investigated [16–18]. Turbulent models were coupled with fluidized bed models [19,20]. The dependency of particle–particle collision on turbulence characteristics, such as turbulent kinetic energy (TKE), dissipation rate (TDR), fluctuation and correlated fluctuations were studied [19]. In order to reduce the computational cost, various effective methods and algorithms were proposed [21–23]. Particle-gas flow of complex geometries was investigated [24,25]. Non-spherical particle collision models were presented [26,27].

Despite many studies on the CFD-DEM modeling of fluidized beds for various applications, only a few studies have been reported on modeling and validation of fluidized beds for concentrated solar reactor/receiver. To the best of our knowledge, the CFD-DEM model of two-tower fluidized bed receiver for beam down solar concentrating system has not been developed and studied considerably. Moreover, as the performance of the two-tower reactor strongly depends on the concentrated radiation (sunlight), the complete flow characteristics of the two-tower receiver is required to improve the design of the receiver. Accordingly, in this study, a CFD-DEM model has been developed to investigate the influence of air flow rate on the flow characteristics, particles flow pattern and velocity of the two-tower reactor. The modeling results have been compared with the experimental results for validation.

## 2. Experimental setup

Recently, couple of fluidized bed reactors have been developed and tested at Niigata University, Japan, for two-step thermochemical water splitting cycles and coal coke gasification using Xe light solar simulator [28–30]. A two-tower fluidized bed system filled with spherical non reacting particles has been proposed as well to use concurrently as receiver and storage system [9]. These fluidized bed systems have been developed for 100 kW<sub>th</sub> beam-down demonstration plant at Miyazaki, Japan, which consists of 88 heliostats with total area of 176 m<sup>2</sup> and an

elliptical reflecting mirror at 16 m height. The schematic of the proposed beam-down reactor/receiver is shown in Fig. 1(a). Both towers filled by spherical particles. The left tower (LT) exposes to the concentrated radiation. Consequently, particles of the left tower receive radiation through the top slit and exchange the thermal energy with other particles and the heat transfer fluid. Subsequently, the heated particles gradually move to the right tower (RT) by fluidization of particles through drag force given by fluid flow with appropriate flow rate conditions at the inlets of left and right towers.

The thermo-chemical reaction/storage of the two-tower reactor strongly depends on the concentrated radiation obtained through the top slit of the LT. The intensity of the radiation is according to the sunlight which depends on the time of the day. Thus, an appropriate flow pattern and the velocity of the circulation should be given according to the sunlight availability (irradiation power). Hence, the complete flow characteristics of the two-tower receiver are required to implement the proposed concept. Thus, in order to investigate the characteristics of circulating flow between the left and right towers and the influence of fluid flow rate on mixing and flow direction (clockwise or anticlockwise), a lab-scale transparent fluidized bed system has been designed and fabricated as shown in Fig. 1(b). As can be seen in the figure, the rectangular shape left tower (60 mm width and depth, and 140 mm height) is extended at the top end as frustum shape to receive radiation through the top slit. In order to prevent the asymmetric effects

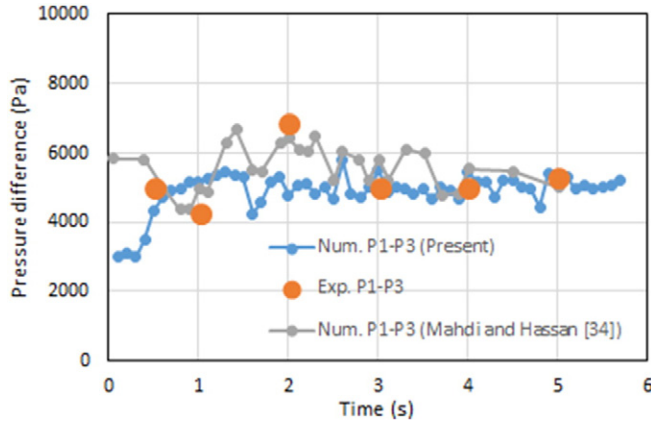
Table 1  
Properties of particles and gas.

Particles	
Shape	Spherical
Density (kg/m <sup>3</sup> )	1040
Coefficient of restitution	0.9
Coefficient of friction	0.3
Total weight of the particles (kg)	0.291
Diameter range (mm)	Mass fraction in range
0.7–0.8	0.82
0.8–0.9	0.03
0.9–1.0	0.03
1.0–1.1	0.03
1.1–1.2	0.03
1.2–1.3	0.03
1.3–1.4	0.03
Gas	
Density (kg/m <sup>3</sup> )	1.225
Viscosity (kg/m-s)	$1.7894 \times 10^{-5}$

**Table 2**

Simulation conditions and operating parameters Mahdi and Hassan [34].

Description	Value
Particle density (kg/m <sup>3</sup> )	2500
Particle diameter (μm)	175, 275, 375
Coefficient of restitution	0.9
Coefficient of friction	0.3
Superficial gas velocity (m/s)	0.38
Diameter of the bed (m)	0.28
Height of the bed (m)	1
Initial Bed Height (m)	0.44
Initial solid packing	0.5
Gas density (kg/m <sup>3</sup> )	1.225
Viscosity (kg/m-s)	$1.7894 \times 10^{-5}$

**Fig. 2.** Pressure drop (P1–P3) comparison of present model and reported experimental and numerical model.

of the flow at the inlet of the bed, the air is injected through a perforated stainless steel plate (20 mm away from the bottom). The right tower consisted of a rectangular duct (40 mm width and depth and 140 mm height) in which a perforated plate is fixed at 45° as shown in the figure. Both towers can interact each other through the top and bottom intersection ports. Polystyrene beads of diameter in the range 0.7 to 1.4 mm are filled in the reactor up to  $z = 0.098$  m. The fluid flow rate difference between the left and right towers determines the direction

of flow circulation. Hence, to study the effect of fluid flow rate on hydrodynamics and the flow pattern of particles, a numerical model has been developed.

### 3. Computational model

A numerical model is developed by the combined approach of computational fluid dynamics (CFD) and discrete element method (DEM) collisional model. The fluid flow of the gas-phase is simulated from the volume-averaged Navier–Stokes equations whereas the motion of every individual particle is tracked by Newton's second law. The particle collisions are modelled based on the soft-sphere method, originally developed by Cundall and Strack [31]. The governing equations to simulate the hydrodynamics and track the particles are summarized below.

The conservation equations of mass and momentum of the fluid phase are;

$$\frac{\partial}{\partial t} (\alpha_f \rho_f) + \nabla \cdot (\alpha_f \rho_f \vec{v}_f) = 0 \quad (1)$$

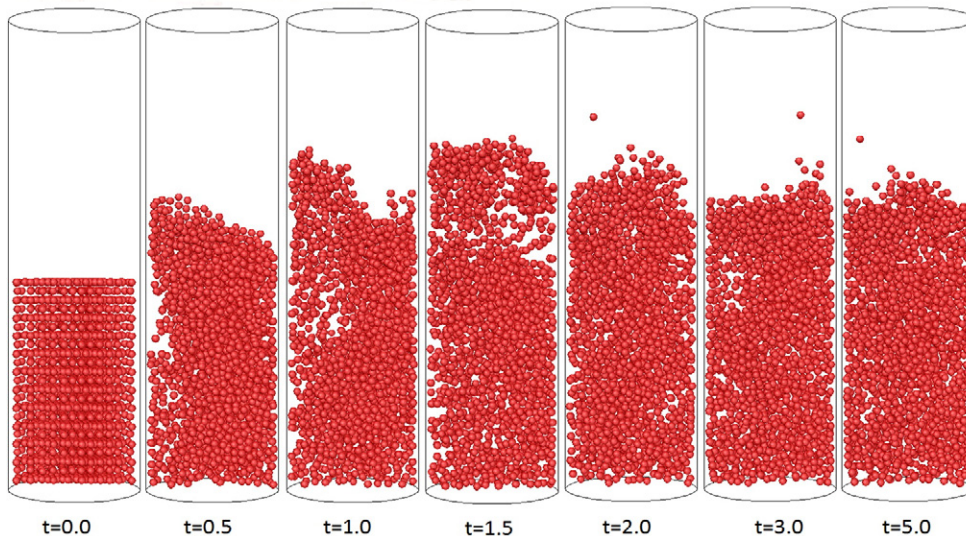
$$\frac{\partial}{\partial t} (\alpha_f \rho_f \vec{v}_f) + \nabla \cdot (\alpha_f \rho_f \vec{v}_f \vec{v}_f) = -\alpha_f \nabla p + \nabla \cdot \overline{\overline{\tau}}_f + \alpha_f \rho_f \vec{g} + S_p \quad (2)$$

where  $\rho$ ,  $\alpha$ ,  $v$ ,  $p$ ,  $\overline{\overline{\tau}}_f$  and  $S_p$  are density, volume fraction, velocity, pressure, stress-strain tensor of fluid phase and the force exerted by the particulate phase respectively. In this model, the moving particles are considered as moving mass points and the fluid flow details around the particles, such as boundary layers, vortex shedding, are neglected. In this Eulerian-Lagrangian model, every particle is tracked by

$$m_p \frac{d\vec{v}_p}{dt} = \frac{V_p \beta}{1 - \alpha_f} (v_f - v_p) + m_p \vec{g} - V_p \nabla p + \vec{F}_c \quad (3)$$

where  $m_p$ ,  $v_p$  and  $V_p$  are mass, velocity and volume of the particle respectively. In order to calculate inter-phase momentum transfer coefficient, several drag models have been developed in the past few decades. In this study, the inter-phase momentum transfer coefficient,  $\beta$ , is computed by the Ergun [32], Wen and Yu [33] correlations for dense regimes and diluted regimes respectively as given below;

$$\beta = 150 \frac{(1 - \alpha_f)^2 \mu}{\alpha_f d_p^2} + 1.75 (1 - \alpha_f) \frac{\rho_g}{d_p} |\vec{v}_f - \vec{v}_p| \quad \text{if } \alpha_f < 0.8 \quad (4)$$

**Fig. 3.** Temporal variation of solid fraction of the bed predicted by present model.



$$\beta = \frac{3}{4} C_D \frac{\alpha_f(1-\alpha_f)}{d_p} \rho_f |\vec{v}_f - \vec{v}_p| \alpha_f^{-2.65} \quad \text{if } \alpha_f > 0.8 \quad (5)$$

The drag coefficient is calculated by

$$C_D = \frac{24}{Re} (1 + 0.15 Re)^{0.687} \quad (6)$$

where  $\mu$  and  $d_p$  are dynamic viscosity and diameter of the particle respectively. A linear-spring and dashpot model is employed to calculate the contact forces ( $\vec{F}_C$ ). The contact force is the accumulation of the normal force ( $\vec{F}_n$ ) and tangential force ( $\vec{F}_t$ ). The contact force is a function of relative velocity and particle overlap, in which the spring and dashpot simulate the deformation effect and damping effect respectively.

$$\vec{F}_n = -k \vec{d}_n - \eta \vec{v}_n \quad (7)$$

$$\vec{v}_n = (\vec{v}_r \cdot \vec{n}) \vec{n} \quad (8)$$

where  $k$  is the stiffness of the spring,  $\eta$  is the coefficient of viscous dissipation,  $n$  is unit vector,  $d_n$  and  $d_t$  are respectively the particle displacements in the normal and tangential directions,  $v_r$  is the relative velocity. The friction collision law, which is based on the equation of coulomb friction, is used to calculate the tangential component of the contact force,

$$F_t = -k \vec{d}_t - \eta \vec{v}_t \quad \text{if } |F_t| \leq \gamma |F_n| \quad (9)$$

$$\vec{F}_t = -\gamma |F_n| \vec{t} \quad \text{if } |F_t| > \gamma |F_n| \quad (10)$$

$$\vec{v}_t = \vec{v}_r - \vec{v}_n \quad (11)$$

where  $\gamma$  and  $t$  are the coefficient of friction and the unit vector respectively. The properties of the particles and gas are given in Table 1. The parameters such as spring stiffness, restitution coefficient and friction coefficient are obtained from the experimental results and literature [13].

The control volume technique was used to solve the governing equations by the commercial software Ansys Fluent. The phase coupled SIMPLE algorithm, which is an extension of the SIMPLE algorithm to multiphase flows, was employed to treat the coupling between pressure and momentum. The QUICK scheme was used to discretize the momentum and void fraction equations. The under relaxation factors for pressure, momentum and volume fraction were 0.9, 0.3, and 1.0, respectively. Scaled absolute residuals of  $10^{-4}$  and  $10^{-6}$  were set as the convergence criteria for continuity and velocity components respectively. As this fluidized bed system consists of more than one million particles, the computational cost of the collision calculation is prohibitive. Thus, in order to reduce the computational cost and track the particles in efficient manner, the parcel concept proposed by Ansys Fluent was used. Parcels are statistical representations of a number of individual particles. In this approach, the dimension of the fluid cell should be sufficiently larger than the parcel size. Based on our experience, if the fluid cell length is less than five times the diameter of the particle ( $< 5d_p$ ), the solution diverges, on the contrary if the fluid cell is too large, the flow field resolution decreases. Hence, the cell length between ( $5d_p$ ) and ( $10d_p$ ) provides a good balance to tackle the aforementioned issues. Attention was paid to the grid parameters such as maximum cell aspect ratio, cell orthogonal quality and cell skewness. Furthermore, the

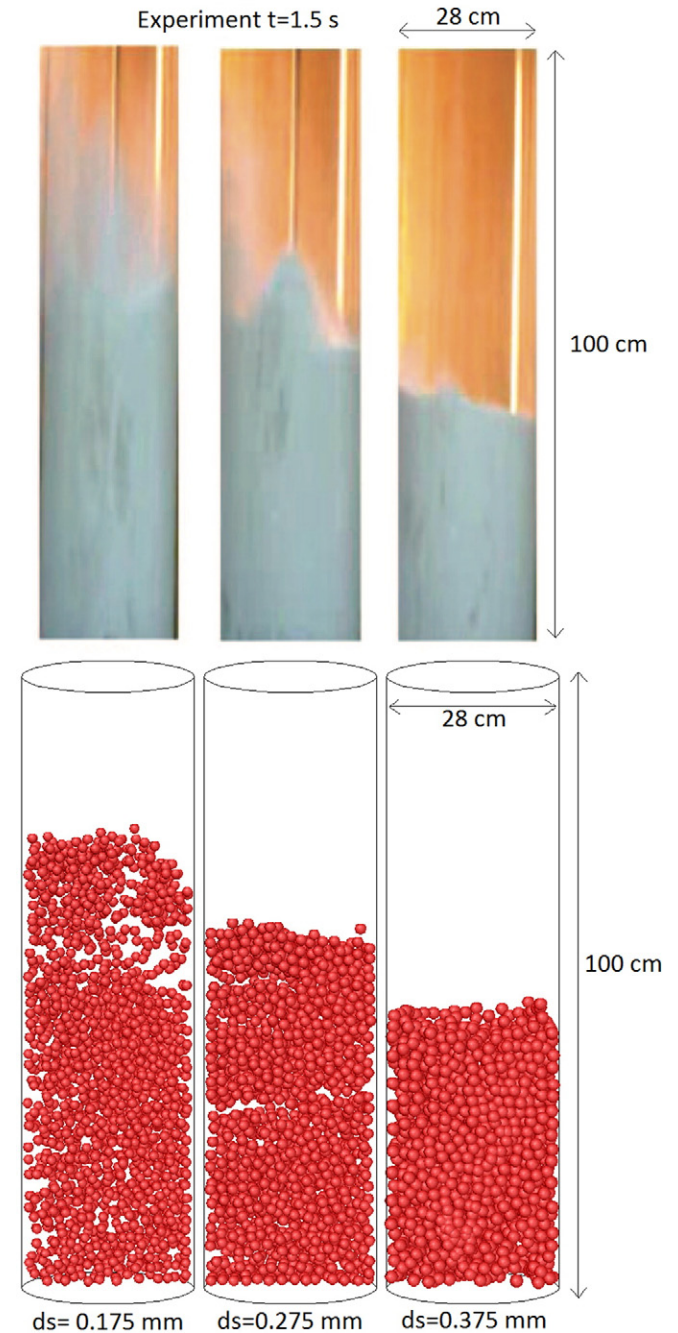


Fig. 4. Solid fraction of the bed predicted by present model and measured by experiments at  $t = 1.5$  s for various particle sizes; 175, 275, 375  $\mu\text{m}$ .

particle time step should be smaller than the CFD time step. In order to obtain stable calculations, the CFD time step was maintained  $< 10$  times of the particle time step. As the soft-sphere collision model is a time step driven model, the particle time step plays a vital role and it should be less than the collisional time scale ( $t_{coll}$ )

$$t_{coll} = \sqrt{\pi^2 + \ln^2 \eta} \sqrt{\frac{m}{k}} \quad (12)$$

where  $m$  is the reduced mass of the parcel.

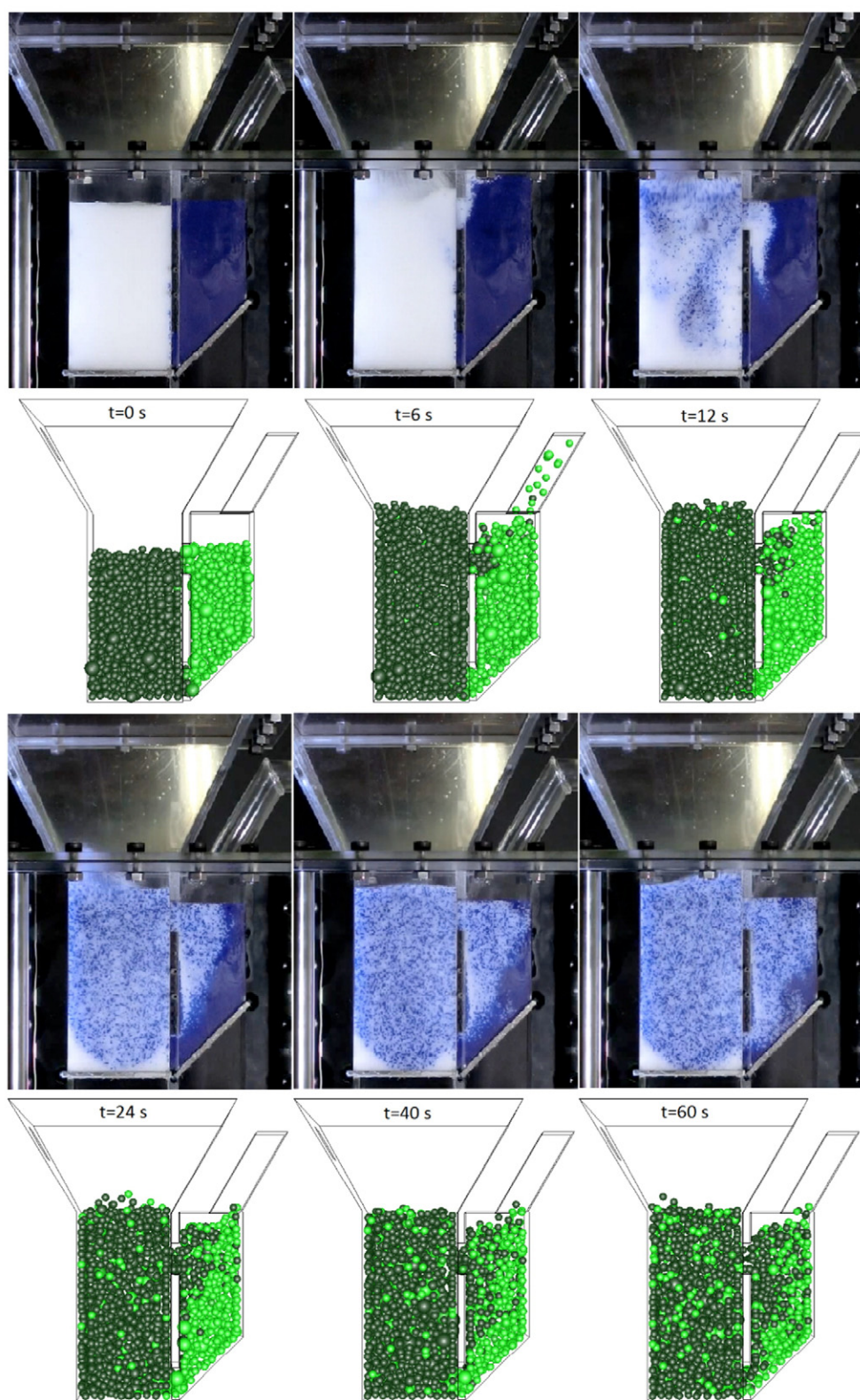


Fig. 5. Comparison of experimentally captured and numerically predicted flow pattern of particles at different times.

## 4. Results and discussion

### 4.1. Model validation

In order to validate the developed model, simulations were performed for the reported study of Mahdi and Hassan [34]. In their

study, the hydrodynamics of the gas-solid fluidized bed reactor was investigated experimentally and numerically for a cylindrical fluidized bed reactor with 100 cm height and 28 cm diameter. Table 2 lists the simulation conditions and model parameters. The uniform gas velocity and pressure-outlet boundary conditions were given at the inlet and outlet respectively. At the walls, no-slip boundary condition for the



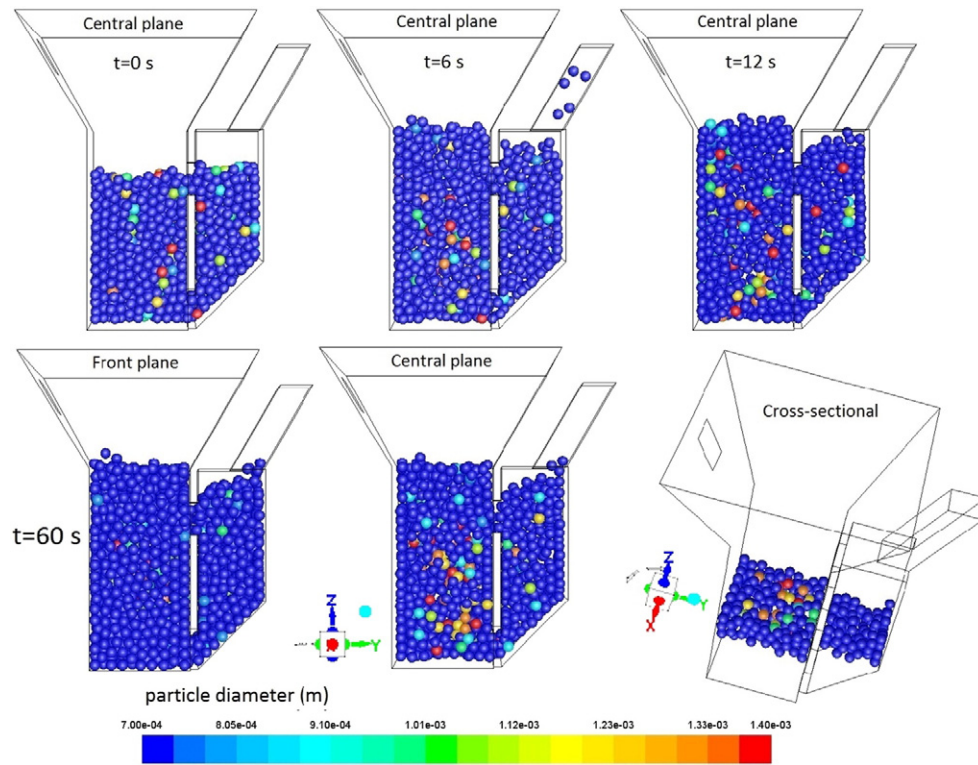


Fig. 6. Influence of particle size on flow characteristics at different stages for case 2.

gas phase was applied. Simulation was performed for the case of particle diameter = 175  $\mu\text{m}$ . The pressure drop (P1–P3) of the bed predicted by the present model, reported model and experimental measurements are compared in Fig. 2. It can be noticed that the pressure drop significantly fluctuates during the initial stage and subsequently reaches almost steady value after 3.0 s. As can be observed, the present model results provide a fair agreement with the experimental results and reported model results. Fig. 3 shows the temporal variation of solid fraction of the bed predicted by present model. At the early stage, the velocity of the gas-phase close to the near-wall region is high, as a result, it creates waves of voidage along the wall and subsequently breaks into bubbles and extends the height of the bed. As shown in Fig. 3, after  $t = 2$  s, the height of the fluidized bed is almost constant.

Fig. 4 shows the comparison of solid fraction of the bed predicted by present model and measured by experiments for various particle sizes; 175, 275, 375  $\mu\text{m}$ . The inlet superficial velocity was same for all cases. As can be seen in Fig. 4, a reasonably good agreement is found between the experimental and numerical results. Then, simulations were performed for the two-tower system. In order to obtain the visualization of movement of particles between the two towers, two colors of polystyrene beads were filled in left (white) and right (blue) towers. The size of the particle typically ranges from 0.7 to 1.4 mm diameter. The shape and properties of the particles are same in both towers; the only variation is the color. The flow rate of the LT and RT were fixed to 70 and 30 (L/min) respectively (case 2). Instantaneous flow and distribution of the particles predicted by model and captured by experiments

are compared in Fig. 5. In simulation results, dark and light green colors represent the white and blue colors particles of the experiments. As the reactor is filled with particles of different sizes, the style attributes of the particles is given by sphere size to emphasize the particle size distribution. As can be seen in the figure, at the early stage, the injected air through the porous plates lifts up the particles by drag force and starts fluidization in both towers. As the fluid velocity of the LT is higher than the RT, the porosity at the bottom region of the LT increases as the particles are lifted up. Simultaneously, as the right tower porous plate is inclined by 45°, the particles in the right tower move to the left tower through the bottom interaction port. Subsequently, the particles in the top region of the left tower gradually move to the right tower through the top interaction port. Thus, the circulation of particles between the two towers occurs in clockwise direction. During the initial stages of experiments, it was observed that a few particles (negligible amount) were left the reactor through the outlet of the RT due to the lack of free space at the top region of the RT. In simulations, as the reflect boundary condition was applied to the discrete phase, the particles were returned to the reactor, which can be observed at  $t = 6$  s. As the time progresses, at the bottom interaction port, only blue color particles from the RT enters into the LT and mixed with white particles. Consequently, the mixed particles (blue and white) from the LT enter into the RT through the top interaction port. However, the ratio of blue particles is much lower than white particles; this effect can be apparently seen at  $t = 12$  s. Subsequently, percentage of blue particles at the LT gradually increases until the mixed particles reach the bottom interaction port through the RT. As the fluidization close to the right near wall region of the RT is very low, the mixing rate is low in that region, which is also noticed in the figure. All in all, the computational results are in good agreement with the experimental results.

Table 3  
Details of operating conditions.

Case	LT flow rate (L/min)	RT flow rate (L/min)
1	30	30
2	70	30
3	100	30
4	30	22
5	30	38

#### 4.2. Effect of particle size

Fig. 6 shows the distribution of particle size at various stages (for case 2) during fluidization to emphasize the effect of particle size and its three-dimensional effect. Initially ( $t = 0$  s), the reactor was filled

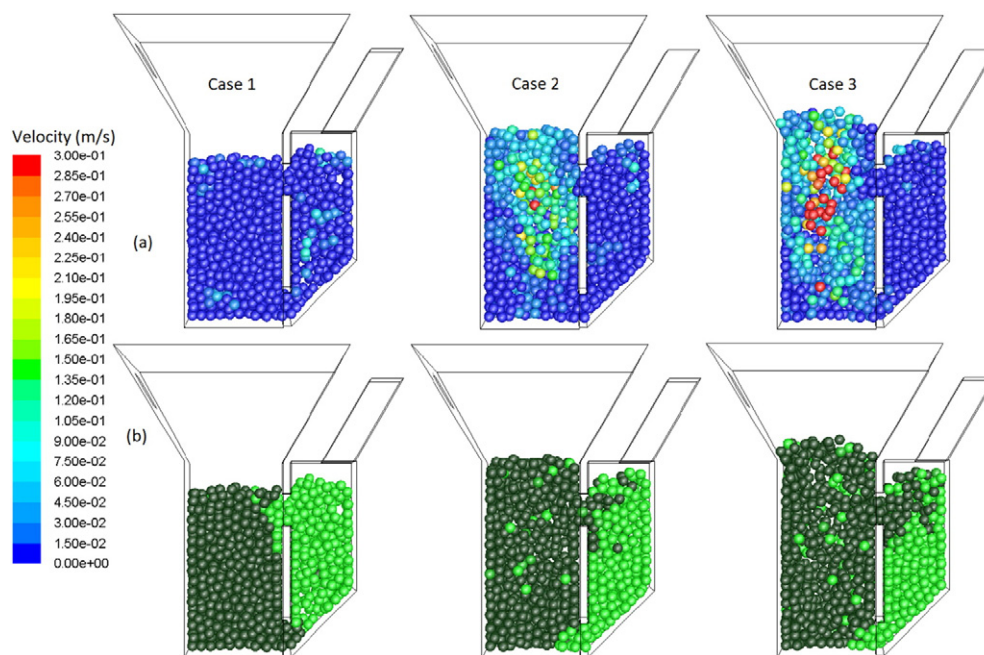


Fig. 7. Influence of LT flow rate on (a) velocity and (b) flow pattern of fluidized particles (central plane) at 15 s for various conditions.

with particles, size in the range between 0.7 and 1.4 mm diameter. The range of particle size was chosen according to the fluidized bed reactors developed at Niigata University for solar thermochemical processes [28–30]. As the velocity of the gas at central axial region is higher than the near wall region, such as parabolic flow, the big size particles penetrate and reach the high velocity region whereas the small size particles occupy the near wall region since the drag force of small particles

inadequate to penetrate the high velocity flow streams [35]. At  $t = 60$  s, it is noticed that almost all large size particles accumulate at the core jet region and induce three dimensional effects. As a result, circulation of granular between the two towers is mainly driven by the small size particles, which is clearly shown by the contour figures at  $t = 60$  s; some portions of the particles are filtered to show the central plane and cross-sectional view.

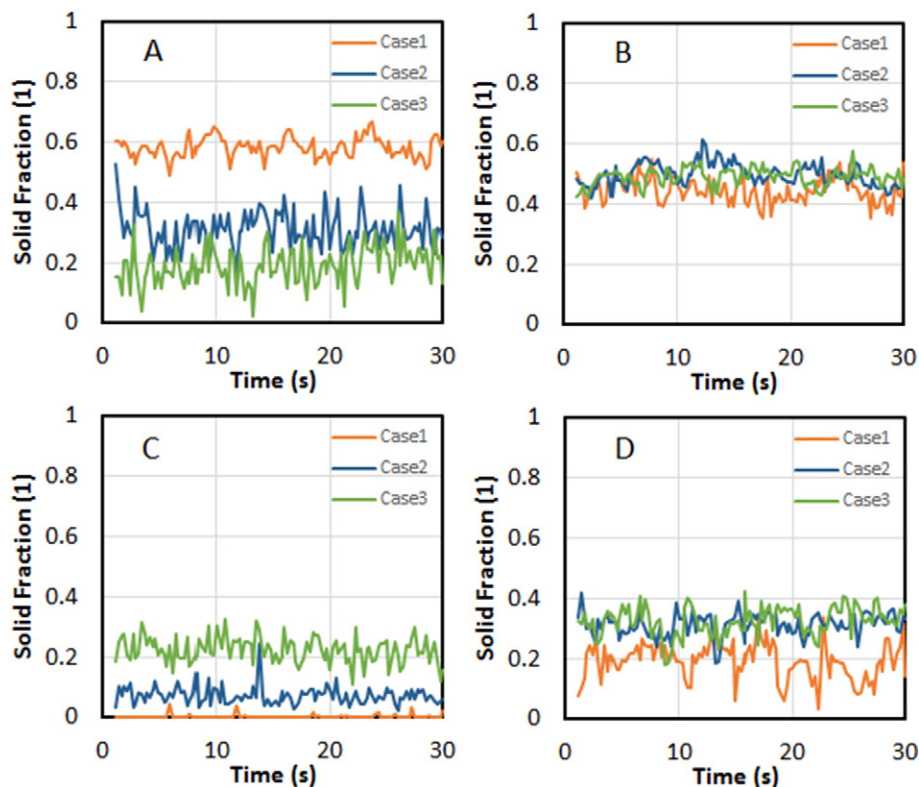


Fig. 8. Solid fraction at various locations predicted over time for various LT flow rates.

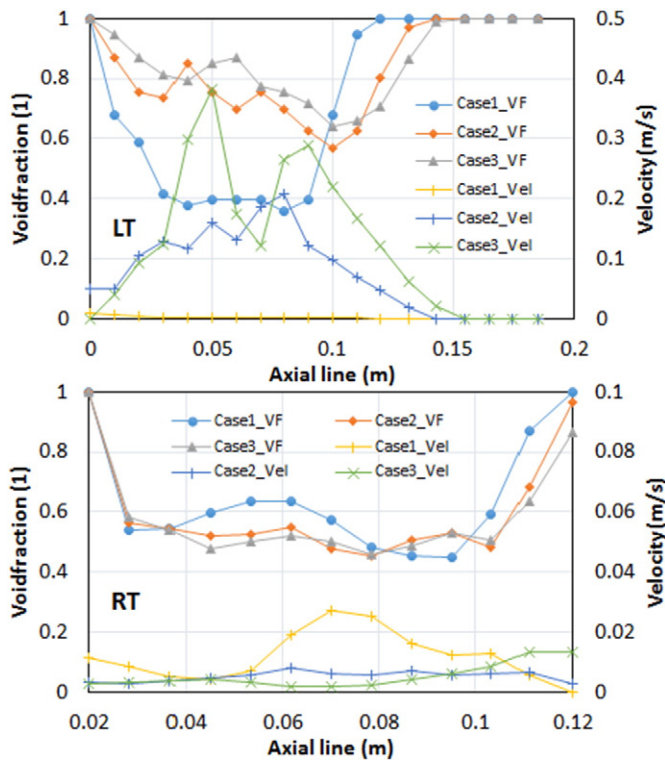


Fig. 9. Void fraction of the bed and velocity of the discrete phase at central axis for various LT fluid flow rates.

#### 4.3. Influence of LT inlet velocity

The validated model was used for simulation of bubbling fluidization with varying the LT fluid flow rate by keeping the RT flow rate and all other parameters constant; the RT was fixed to 30 L/min, while the LT flow rate for each simulation was varied from 30 L/min to 100 L/min as given in Table 3 (cases 1, 2 and 3). Fig. 7 shows the central plane view of velocity and flow pattern (two colors of particles) of particulate phase for different cases at  $t = 15$  s. In case1, the velocity of the fluid at LT is lower than the RT, as a result, the fluidization occurs in anticlockwise direction. In cases 2 and 3, as the mass flow rate of LT is higher than RT, the velocity of the particulate phase of LT is higher than RT. Hence, the fluidization occurs in clockwise direction, which is apparently noticed in the figure.

Fig. 8 shows the solid fraction of the reactor at different locations as a function of time. The positions A and C are at the central axis region of the LT; 60 mm and 130 mm from the bottom perforated plate respectively (as shown in Fig. 1). The positions B and D are at the central axis

area of the RT; 60 mm and 110 mm from the bottom perforated plate respectively. When increasing the LT flow rate, the drag force on the particles increases, as a result, the fluid lifts up the particles and expands the bed height. The average bed height of the LT increased by 5, 22 and 31 mm for case 1, case 2 and case 3 respectively. Thus, the solid fraction at the center (position A) and top part (C) of the LT are decreasing and increasing respectively as the LT mass flow rate increases. As aforementioned, cases 2 and 3 lead the particulate phase in clockwise direction, accordingly, bring some particles from LT to RT through top interaction port. Furthermore, a portion of the fluid from the LT passes through the RT and leaves the reactor through the RT outlet. Hence, the solid fraction at the top part of the RT (position D) increases with increasing the LT flow rate.

Fig. 9 shows the void fraction of the bed and velocity of the discrete phase at the central axis of LT and RT for different cases at  $t = 30$  s. It is noticed in the LT that the velocity of the particles significantly increases when increasing the flow rate from 30 L/min to 100 L/min. Consequently, the porosity of the bed increases throughout the bed, especially in the region between  $z = 0.03$  and  $z = 0.1$  m. As anticipated, the porosity and the particles velocity of the RT are not significantly changed when comparing with the LT. However, the higher mass flow rate of LT slightly decreases the void fraction and velocity of the particles at the RT. This is because of the rate of particle transfer at the top and bottom interaction ports. During the initial stage, the number of particles transfer from the RT to LT is relatively low at the bottom interaction port since the high velocity of the LT gas resists the right tower particles to penetrate into the left tower. Concurrently, the total number of particles moving from LT into RT is comparatively higher at the top interaction port since the velocity of LT is higher than the RT, hence, which increases the solid fraction of the RT and the volumetric gravitational force. Consequently, after a few seconds, the total number of particles transfer between the LT and RT at the bottom and top interaction ports are almost equal.

#### 4.4. Influence of RT inlet velocity

To study the effect of the RT fluid flow rate on the velocity and flow distribution of the particulate phase, simulations were performed for cases 1, 4 and 5 as given in Table 3. By keeping the LT fluid flow rate constant, the RT flow rate was varied from 22 L/min to 38 L/min. As the fluid velocity of the RT is higher than the LT, these cases lead the particulate flow in anticlockwise direction. Fig. 10 shows the flow pattern of the two colors particulate phase for different cases at  $t = 15$  s. As can be seen in the figure, the rate of particles transfer between the RT and LT significantly increases with increase in flow rate of the RT. Hence, the circulation velocity of the two-tower bed increases.

Fig. 11 shows the temporal variation of solid fraction at different locations of the bed for different RT air flow rates. As seen in Fig. 11, when increasing the RT fluid flow rate, the solid fraction at the center (Point-B) and top (Point-D) regions of the RT are decreasing and

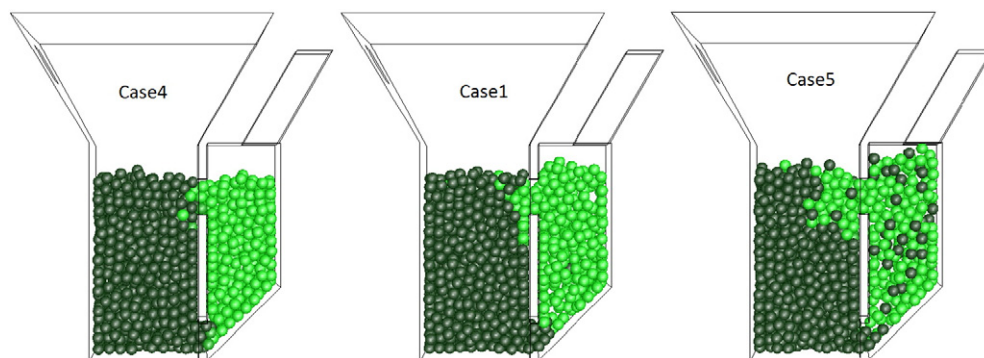


Fig. 10. Flow pattern of two-color fluidized bed for different RT flow rates at 15 s.



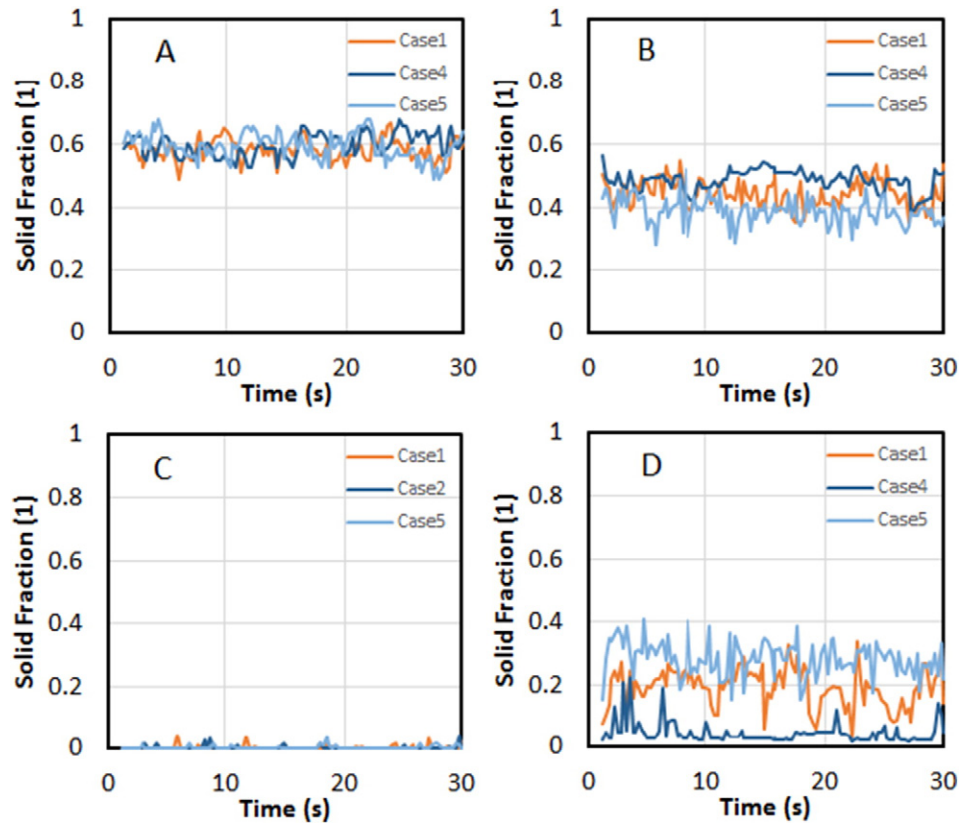


Fig. 11. Influence of RT inlet velocity on solid fraction at different locations over time.

increasing respectively, due to particulate phase flow pattern. As expected, the solid fraction of the LT is not significantly influenced by the inlet velocity of RT (in the given range). Fig. 12 shows the void

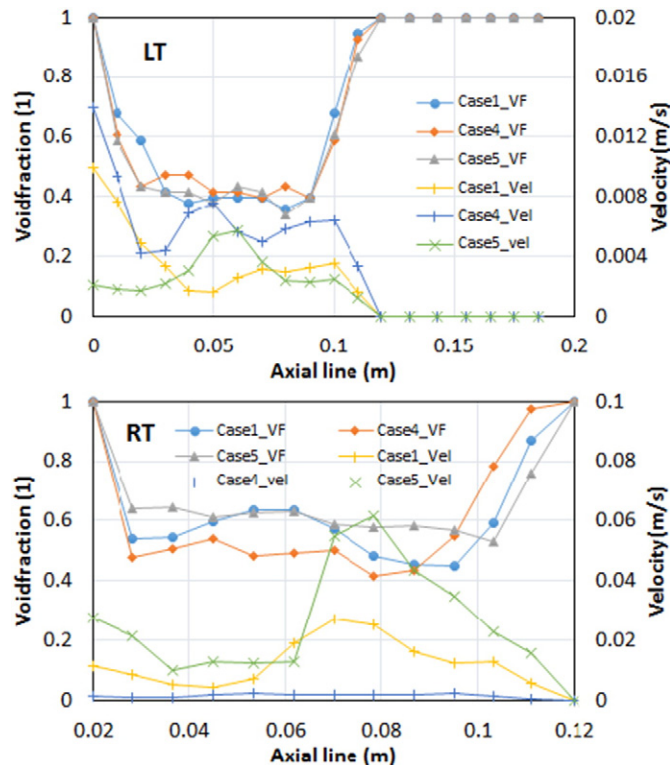


Fig. 12. Void fraction of the bed and velocity of the discrete phase at central axis for various RT inlet velocity.

fraction and velocity of the particles at central axis of the LT and the RT for various air flow rates. The results show that, the higher mass flow rate of the RT increases the void fraction and velocity of the particles at the RT, especially in the region between  $z = 0.03$  m and  $z = 0.09$  m. In the given range, the results of the LT are not significantly influenced by the RT air flow rate.

## 5. Conclusion

A three dimensional Eulerian-Lagrangian model has been developed to study the flow pattern, velocity distribution and circulating velocity of the receiver. An experimental visualization of particles circulation pattern and mixing of two-tower fluidized bed system has been presented. The model has been validated using the experimental results and the reported model results. Using the well-defined experiments with the CFD-DEM model, the flow characteristics of the particulate phase for various conditions have been studied. The important results obtained from this study are summarized as follows.

The flow pattern has three dimensional effects due to particle size; the large size particles are accumulated at the central axis region of the left and right towers. Circulation of granular between the two towers is predominantly driven by the small particles. The fluid flow rate significantly influences the flow characteristics in the region between  $z = 0.03$  m and  $z = 0.1$  m. The influence of LT inlet velocity on the RT particle flow characteristics (porosity and velocity), and vice versa, is not significant. The average height of the bed increased by 23.4% when increasing the air flow rate of the LT about 70%.

The developed numerical model, consists of Ergun and Wen-Yu drag model and linear-spring and dashpot model, provides the flow pattern and flow distribution similar to the experimental results of two-tower receiver. Hence, this model is capable to describe the experimentally observed flow characteristics. Using this model, according to the sunlight availability (irradiation power), an appropriate flow pattern, direction (clockwise or anticlockwise) and the velocity of the circulation can

be predicted and optimized by the fluid flow rates of LT and RT. This model can be used to improve the design of the two-tower type fluidized bed receivers for beam-down concentrating system.

## Acknowledgement

This study has been supported by the Tenure Track Program, The Ministry of Education, Culture, Sports, Science and Technology of Japan.

## References

- [1] M.Z. Jacobson, Review of solutions to global warming, air pollution, and energy security, *Energy Environ. Sci.* 2 (2009) 148–173.
- [2] T. Kodama, N. Gokon, Thermochemical cycles for high-temperature solar hydrogen production, *Chem. Rev.* 107 (2007) 4048–4077.
- [3] World Energy Outlook, IEA (International Energy Agency), <http://www.worldenergyoutlook.org> 2014.
- [4] P. Salatino, P. Ammendola, P. Bareschino, R. Chirone, R. Solimene, Improving the thermal performance of fluidized beds for concentrated solar power and thermal energy storage, *Powder Technol.* 290 (2016) 97–101.
- [5] G. Flamant, D. Gauthier, C. Boudhari, Y. Flitris, A 50 kW fluidized bed high temperature solar receiver: heat transfer analysis, *J. Sol. Energy Eng.* 110 (1988) 313–320.
- [6] B. Sakadjian, S. Hu, M. Maryamchik, T. Flynn, K. Santelmann, Z. Ma, Fluidized-bed technology enabling the integration of high temperature solar receiver CSP systems with steam and advanced power cycles, *Energy Procedia* 69 (2015) 1404–1411.
- [7] R. Ansart, P. García-Triñanes, B. Boissière, H. Benoit, J.P.K. Seville, O. Simonin, Dense gas-particle suspension upward flow used as heat transfer fluid in solar receiver: PEPT experiments and 3D numerical simulations, *Powder Technol.* 307 (2017) 25–36.
- [8] K. Matsubara, Y. Kazuma, A. Sakurai, S. Suzuki, L. Soon-Jae, T. Kodama, N. Gokon, High-temperature fluidized receiver for concentrated solar radiation by a beam-down reflector system, *Energy Procedia* 49 (2014) 447–456.
- [9] K. Matsubara, H. Sakai, Y. Kazuma, A. Sakurai, T. Kodama, N. Gokon, H.S. Cho, K. Yoshida, Numerical modeling of a two-tower type fluidized receiver for high temperature solar concentration by a beam-down reflector system, *Energy Procedia* 69 (2015) 487–496.
- [10] A. Steinfeld, Solar thermochemical production of hydrogen—a review, *Sol. Energy* 78 (2005) 603–615.
- [11] J.R. Van Ommen, R.F. Mudde, Measuring the gas-solids distribution in fluidized beds – a review, *Int. J. Chem. React. Eng.* 6 (2008) 1542–1580.
- [12] G.A. Bokkers, M. van Sint Annaland, J.A.M. Kuipers, Mixing and segregation in a bidisperse gas–solid fluidised bed: a numerical and experimental study, *Powder Technol.* 140 (2004) 176–186.
- [13] Y. Tsuji, T. Kawaguchi, T. Tanaka, Discrete particle simulation of two-dimensional fluidized bed, *Powder Technol.* 77 (1993) 79–87.
- [14] G. Zhang, M. Gutierrez, M. Li, A coupled CFD-DEM approach to model particle-fluid mixture transport between two parallel plates to improve understanding of proppant micromechanics in hydraulic fractures, *Powder Technol.* 308 (2017) 235–248.
- [15] J. Zhou, C. Du, S. Liu, Y. Liu, Comparison of three types of swirling generators in coarse particle pneumatic conveying using CFD-DEM simulation, *Powder Technol.* 301 (2016) 1309–1320.
- [16] Q.F. Hou, Z.Y. Zhou, A.B. Yu, Computational study of heat transfer in a bubbling fluidized bed with a horizontal tube, *AIChE J.* 58 (2012) 1422–1434.
- [17] Y. Zhao, M. Jiang, Y. Liu, J. Zheng, Particle-scale simulation of the flow and heat transfer behaviors in fluidized bed with immersed tube, *AIChE J.* 55 (2009) 3109–3124.
- [18] T. Tsory, N.B. Jacob, T. Brosh, A. Levy, Thermal DEM–CFD modeling and simulation of heat transfer through packed bed, *Powder Technol.* 244 (2013) 52–60.
- [19] N. Gui, J.R. Fan, S. Chen, Numerical study of particle–particle collision in swirling jets: a DEM–DNS coupling simulation, *Chem. Eng. Sci.* 65 (2010) 3268–3278.
- [20] W. Zhong, Y. Xiong, Z. Yuan, M. Zhang, DEM simulation of gas–solid flow behaviors in spout-fluid bed, *Chem. Eng. Sci.* 61 (2006) 1571–1584.
- [21] S. Benyahia, J.E. Galvin, Estimation of numerical errors related to some basic assumptions in discrete particle methods, *Ind. Eng. Chem. Res.* 49 (2010) 10588–10605.
- [22] M.A. Mokhtar, K. Kuwagi, T. Takami, H. Hirano, M. Horio, Validation of the similar particle assembly (SPA) model for the fluidization of Geldart's group A and D particles, *AIChE J.* 58 (2012) 87–98.
- [23] H.R. Norouzi, R. Zarghami, N. Mostoufi, New hybrid CPU-GPU solver for CFD-DEM simulation of fluidized beds, *Powder Technol.*, 316 (2017) 233–244. <http://dx.doi.org/10.1016/j.powtec.2016.11.061>.
- [24] K.W. Chu, B. Wang, D.L. Xu, Y.X. Chen, A.B. Yu, CFD–DEM simulation of the gas–solid flow in a cyclone separator, *Chem. Eng. Sci.* 66 (2011) 834–847.
- [25] S.B. Kuang, A.B. Yu, Micromechanic modeling and analysis of the flow regimes in horizontal pneumatic conveying, *AIChE J.* 57 (2011) 2708–2725.
- [26] F. Geng, Y. Li, X. Wang, Z. Yuan, Y. Yan, D. Luo, Simulation of dynamic processes on flexible filamentous particles in the transverse section of a rotary dryer and its comparison with video-imaging experiments, *Powder Technol.* 207 (2011) 175–182.
- [27] D. Höhner, S. Wirtz, H. Kruggel-Emden, V. Scherer, Comparison of the multi-sphere and polyhedral approach to simulate non-spherical particles within the discrete element method: influence on temporal force evolution for multiple contacts, *Powder Technol.* 208 (2011) 643–656.
- [28] N. Gokon, T. Mataga, N. Kondo, T. Kodama, Thermochemical two-step water splitting by internally circulating fluidized bed of NiFe<sub>2</sub>O<sub>4</sub> particles: successive reaction of thermal-reduction and water-decomposition steps, *Int. J. Hydrog. Energy* 36 (2011) 4757–4767.
- [29] T. Kodama, N. Gokon, S. Enomoto, S. Itoh, T. Hatamachi, Coal coke gasification in a windowed solar chemical reactor for beam-down optics, *Journal of Solar Energy Engineering* 132 (2010) 1–6, 041004.
- [30] N. Gokon, T. Izawa, T. Abe, T. Kodama, Steam gasification of coal cokes in an internally circulating fluidized bed of thermal storage material for solar thermochemical processes, *Int. J. Hydrog. Energy* 39 (2014) 11082–11093.
- [31] P.A. Cundall, D.L. Strack, A discrete numerical model for granular assemblies, *Geotechnique* 29 (1979) 47.
- [32] S. Ergun, Fluid flow through packed columns, *Chem. Eng. Prog.* 48 (1952) 89–94.
- [33] Y.C. Wen, Y.H. Yu, Mechanics of fluidization, *Chem. Eng. Prog. Symp. Ser.* 62 (1966) 100–111.
- [34] H. Mahdi, R. Hassan, Experimental and numerical study of hydrodynamics with heat transfer in a gas–solid fluidized-bed reactor at different particle sizes, *Ind. Eng. Chem. Res.* 48 (2009) 3177–3186.
- [35] S. Yugeswaran, A. Kobayashi, B. Selvan, P.V. Ananthapadmanabhan, In-flight behavior of lanthanum zirconate (La<sub>2</sub>Zr<sub>2</sub>O<sub>7</sub>) particles in gas tunnel type plasma jet and its coating properties, *Vacuum* 88 (2013) 139–143.

## Nomenclature

$d_p$ : diameter of the particle (m)  
 $v$ : velocity (m/s)  
 $p$ : pressure (Pa)  
 $V_p$ : volume of the particle (m<sup>3</sup>)  
 $m_p$ : mass of the particle (kg)  
 $m$ : reduced mass of the particle (kg)  
 $S_p$ : particle-gas momentum exchange (Pa)  
 $k$ : stiffness (N/m)  
 $Re$ : Reynolds number  
 $t$ : time (s)  
 $z$ : axial coordinate (m)

## Greek symbols

$\alpha$ : volume fraction  
 $\beta$ : inter-phase momentum transfer coefficient (kg/(m<sup>3</sup> s))  
 $\gamma$ : coefficient of friction  
 $\mu$ : dynamic viscosity (Pa·s)  
 $\rho$ : density (kg/m<sup>3</sup>)  
 $\tau$ : stress tensor (Pa)

## Subscripts

$f$ : fluid  
 $p$ : particle

## Abbreviations

CFD: computational fluid dynamics  
 DEM: discrete element method  
 CSP: concentrated solar power  
 HTM: heat transfer medium  
 SPR: solar particle receivers  
 DNS: direct numerical simulation  
 TKE: turbulent kinetic energy  
 TDR: dissipation rate  
 LT: left tower  
 RT: right tower  
 LTES: latent thermal energy storage  
 NREL: national renewable energy laboratory  
 PCM: phase change material  
 TES: thermal energy storage